Reynolds-Stress Enhancement Associated with a Short Fetch of Roughness in Wall Turbulence

Y. Wu and K. T. Christensen
University of Illinois at Urbana–Champaign, Urbana, Illinois 61801

Particle-image velocimetry experiments are performed to study the response of smooth-wall turbulent channel flow to a short fetch of roughness (10 outer length scales long). The roughness studied herein is replicated from a surface scan of a damaged turbine blade and contains both large- and small-scale surface defects attributable to pitting, deposition, and spallation. Quadrant analysis is used to investigate the characteristics of Reynolds-stress-producing events within the internal layer that develops over the roughness. The mean Reynolds stress is dramatically increased in the presence of the roughness as compared to the smooth-wall baseline owing to an increased number of extremely intense ejections and sweeps. In contrast, inward and outward interactions, as well as relatively weak ejection and sweep events, are found to be insensitive to the surface conditions. While stress and space fractions are found to be insensitive to the surface topology when all Reynolds-stress-producing events are included, stress and space fractions for only the most intense ejection and sweep events vary significantly with the local surface topology.

Nomenclature

H	=	hyperbolic hole size
h	=	channel half-height, m
I	=	indicator function
k	=	roughness height, m
M	=	total number of streamwise gridpoints in an ensemble
N	=	space fraction
Re_τ	=	friction Reynolds number
S	=	stress fraction
u	=	fluctuating streamwise velocity, m/s
$\tilde{u}$	=	total streamwise velocity, m/s
u_τ	=	friction velocity, m/s
uv	=	instantaneous Reynolds shear stress, m²/s²
v	=	fluctuating wall-normal velocity, m/s
$\tilde{v}$	=	total wall-normal velocity, m/s
x	=	streamwise direction, m
y	=	wall-normal direction, m
y_*	=	viscous length scale, m
z	=	spanwise direction, m
α	=	ratio of ejections to sweeps
Δ	=	PIV grid spacing, m
ν	=	kinematic viscosity of fluid, m²/s
ρ	=	density of fluid, kg/m³
τ_w	=	wall shear stress, Pa

Subscripts

j	=	variable number
max	=	maximum value
Q	=	quadrants (1–4) in the u–v plane

Superscripts

SM	=	smooth-wall value
+	=	normalization in inner units

Symbol

$\langle \cdot \rangle$	=	ensemble and streamwise average

I. Introduction

IT is well known that an abrupt transition from smooth-to-rough surface conditions in a wall-bounded flow promotes the formation of an internal roughness layer that grows in thickness downstream [1]. In such situations, the turbulence intensities and Reynolds shear stress are unaffected except within the internal layer where they can be altered significantly by the surface roughness ([2,3], among others). Such abrupt transitions occur frequently in actual engineering systems where the surface conditions can vary significantly in the dominant flow direction. Many studies have been performed in the presence of rather idealized roughness conditions, like sand grain, ordered arrays of elements, and woven mesh. However, roughness encountered in most practical engineering applications is quite distinct from these idealized roughness models. The surface conditions in such flows can degrade over time, from hydraulically smooth before deployment to significantly roughened over time due to harsh operating conditions, like damage imparted to turbine blades [4,5] or cumulative algae/barnacle buildup on the surfaces of submarines and ships [6], for example. In the case of damaged turbine blades, surface roughness is attributable to deposition of foreign materials, pitting, and spallation, rendering the surface conditions highly nonuniform. As such, a single roughness type and scale cannot be expected to be a sufficient representation of real roughness. In particular, Bons [5] used scaled replicas of turbine-blade roughness in turbulent boundary layer studies and found that classical rough-wall scalings for skin friction derived from simulated roughness do not hold for some real roughness conditions. Therefore, it is not clear whether studying the influence of idealized roughness conditions on wall-bounded turbulence will be sufficient for successfully modeling and controlling flows of practical engineering interest in which the surface conditions are less than ideal.

Quadrant analysis [7,8], first introduced over 30 years ago, allows one to investigate the strongest Reynolds-stress-producing events in turbulent flows. This method decomposes the mean Reynolds shear stress, $\langle uv \rangle(y)$, outside of a hyperbolic hole region of size H into four distinct Reynolds-stress-producing events based on the quadrant in the u–v plane, Q, in which they reside. These events include outward interactions (Q_1: $u > 0, v > 0$), ejections (Q_2: $u < 0, v > 0$), inward interactions (Q_3: $u < 0, v < 0$), and sweeps (Q_4: $u > 0, v < 0$). This decomposition methodology has been used extensively to

study the Reynolds-stress-producing events in turbulent boundary layers as well as turbulent channel and pipe flows. In the wall region of a smooth-wall (SM) turbulent channel flow, Wallace et al. [7] found that ejections and sweeps represented the dominant Reynolds-stress-producing events, with each contributing nearly 70% to the total Reynolds stress at $y^+ \simeq 15$ whereas inward and outward interactions each yielded 20% contributions. Their results also indicated that below $y^+ \simeq 15$ the sweeps and outward interactions were more dominant while outside this region ejections and inward interactions became more important contributors. By comparing the joint probability density distributions of the streamwise (u) and wall-normal (v) fluctuating velocities with the Reynolds-stress-contribution distributions, Wallace and Brodkey [9] concluded that most of the Reynolds stress is generated by the large, energetic motions. Teitel and Antonia [10] applied quadrant analysis to investigate the interaction region of a turbulent channel flow and their results indicated that ejections originating on one side of the centerline can often reach the opposing wall. Finally, Sabot and Comte-Bellot [11] studied the intermittent coherent structures in the core region of a smooth-wall turbulent pipe flow and determined that ejections dominated the wall region.

Quadrant analysis has also been used to assess differences between the Reynolds-stress-producing events in smooth- and rough-wall flows. Grass [12] investigated intermittent ejections and sweeps in rough-wall boundary layers using hydrogen bubble visualization and found that the entrainment of low momentum fluid trapped between the roughness elements was much more violent than the entrainment of the smooth-wall viscous sublayer fluid. Raupach [13] observed that sweeps accounted for most of the turbulent stress near rough surfaces and that the relative magnitude of the sweep component increased both with surface roughness and with proximity to the surface. Similarly, Krogstad et al. [14] observed that contributions from sweeps were significantly greater over rough surfaces (wire mesh) than over smooth surfaces, particularly in the near-wall region. They also found that strong ejections and sweeps occurred almost twice as frequently in the presence of surface roughness. More recently, Demare et al. [15] observed that ejections accounted for 80% of the total Reynolds stress for flow over a smooth wall but only 60–65% in the presence of a rough wall composed of two-dimensional square bars. Further, recent direct numerical simulations (DNS) and experiments by Krogstad et al. [16] in a channel flow roughened on both walls with square bars showed little influence of roughness on the Reynolds stress outside the roughness sublayer ($y > 5k$), particularly in the ratio of ejection to sweep contributions for intermediate roughness heights. This behavior is consistent with the experiments of Flack et al. [17] for flow over sandpaper and wire mesh where the ratio of ejections to sweeps was found to be insensitive to surface roughness in the outer layer. In contrast, the experiments of Nakagawa and Hanratty [18] over wavy walls in channel flow indicate that this ratio is strongly influenced by surface roughness well outside the roughness sublayer for roughness heights beyond the intermediate regime. However, it should be noted that all of these studies involved long streamwise fetches of roughness (exceeding 50 outer length scales in all cited cases) for which the internal roughness layer grew sufficiently to occupy the entire wall-normal domain of the flow (streamwise fetches smaller than that required to achieve such behavior are necessarily classified as "short").

The present effort assesses the Reynolds-stress enhancement associated with a short streamwise fetch of highly irregular surface roughness replicated from a damaged turbine blade using quadrant analysis. Both the impact of highly irregular surface conditions on wall turbulence as well as the character of rough-wall flow over short fetches of roughness have received little attention in the literature despite their vital importance in many practical engineering flows. These issues are therefore the focus of this work.

II.   Experiment

The channel-flow facility used in the present effort has a development length of $216h$ (where $h = 25.4$ mm is the half-height of the channel) and an aspect ratio of 10.125:1, yielding two-dimensional flow along the channel's spanwise centerline. The working fluid of the channel is air and the flow is suitably conditioned upstream of the channel entrance by a series of screens, honeycomb, and a contraction. The flow is then tripped with 36-grit sandpaper, ensuring fully developed conditions at the test section (the flow quality of this channel has been well documented in past turbulence studies [19,20]). Static pressure taps are mounted along the length of the channel's development section to evaluate τ_w. Density and viscosity are assessed from measurements of the atmospheric pressure and fluid temperature and are then used to determine the smooth-wall friction velocity, $u_\tau \equiv (\tau_w/\rho)^{1/2}$, and the viscous length scale, $y_* \equiv \nu/u_\tau$.

The roughness studied herein is quite distinct from other roughness conditions presented in the literature, some of which are cited in the Introduction. The present effort focuses on roughness replicated from a surface scan of a damaged turbine blade (denoted surface 3 in Bons [5]). The surface imperfections often encountered on these blades are attributable to deposition of foreign material, pitting, and spallation, all of which render the surface conditions highly nonuniform. Therefore, a single roughness type and scale, such as those extensively cited in the literature, cannot be expected to be a sufficient representation of this form of "real" roughness. This particular scan was chosen from the six scans discussed in Bons [5] because it embodies both large- and small-scale topological features. Figure 1 presents a contour plot of the surface topology at the downstream end of the roughness insert, illustrating the highly nonuniform surface conditions. A file containing the topological data is input into a three-dimensional printer with 80 μm resolution which constructs a physical replica of the roughness layer by layer. A smooth leading edge of length $0.75h$ transitions the flow from the smooth- to the rough-wall conditions and the surface topology is periodically extended in both the streamwise and the spanwise directions to fill the entire insert area, consistent with the replications of Bons [5]. The average peak-to-valley roughness height, often used as an estimate of k [5], is 1.35 mm, yielding $h/k = 18.8$.

A new test section was designed and constructed allowing a roughness insert to be placed flush along the bottom wall of the channel. The surface roughness is first mounted on a cast aluminum plate which then rests upon three screws within the test section that allow one to adjust the mean elevation of the roughness to be coincident with the upstream smooth wall. The insert is $10h$ long in the streamwise direction but spans the entire width of the channel. As such, these measurements represent the influence of a short fetch of highly irregular roughness on the character of fully developed turbulent channel flow. Further, while the roughness insert impedes optical access from below, such access is still achieved with glass windows embedded in the top and sidewalls of the channel (above and on both sides of the roughness insert, respectively). Smooth-wall measurements are achieved with an anodized cast aluminum plate inserted in place of the roughness panel. Figure 2 presents a schematic of the experimental arrangement.
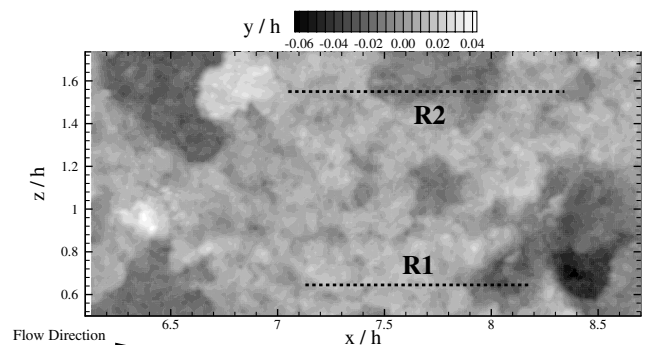

Fig. 1   **Contour plot of the surface topology of the replicated turbine-blade roughness. The abscissa indicates the position relative to the leading edge of the roughness panel and the dashed lines demarcate the streamwise–wall-normal planes where PIV measurements are made.**
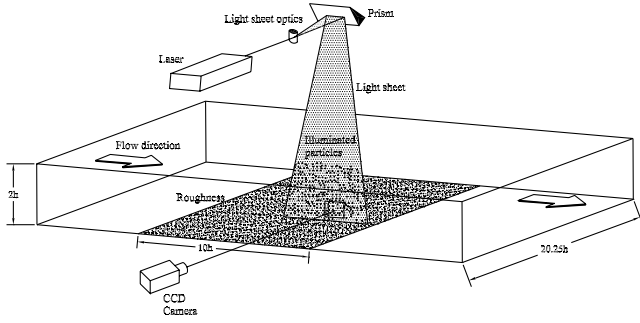
Fig. 2   Schematic of experimental setup.

Particle-image velocimetry (PIV) is used to measure two-dimensional velocity $(\tilde{u}, \tilde{v})$ fields over an $h \times h$ field of view in the streamwise–wall-normal plane along the channel's spanwise center for SM conditions SM and two spanwise separated rough-wall positions (R1 and R2), the latter of which are illustrated in Fig. 1. These two spanwise positions were chosen to assess how distinct local surface features exert their influence upon the flow. Position R1 occurs over relatively small-scale roughness while position R2 is just downstream of a step in surface height from a large-scale, deep depression to a plateau. The air flow in the channel is seeded with 1 μm olive-oil droplets, a dual-cavity Nd:Yag laser is used for illumination, and the scattered light from the particles is imaged with an 8-bit 1 k × 1 k cross-correlation CCD camera. The pairs of PIV images are interrogated using two-frame cross-correlation methods with first-interrogation windows of size 18 × 18 pixels (streamwise × wall normal) at 50% overlap to satisfy Nyquist's criterion. These parameters yield vector grid spacings of $\Delta = 18.9 y_*^{\mathrm{SM}}$, $19.8 y_*^{\mathrm{SM}}$, and $21.0 y_*^{\mathrm{SM}}$ in both the streamwise and wall-normal directions for cases SM, R1, and R2, respectively. A larger second window of 24 × 22 pixels is chosen to minimize bias errors associated with loss of particle pairs and the second window is offset in the mean flow direction by the bulk displacement of the flow to further increase the fidelity of the correlation. The resulting vector fields are then validated using standard deviation and magnitude difference comparisons to remove any erroneous velocity vectors. On average, 97–99% of the velocity vectors in any given velocity realization are found to be valid, minimizing the need for interpolation of holes. Finally, each velocity field is low pass filtered with a narrow Gaussian filter to remove noise associated with frequencies larger than the sampling frequency of the interrogation.

The measurements are performed at the same friction Reynolds number $(Re_\tau \equiv u_\tau h / \nu)$ based on the upstream smooth-wall flow conditions of approximately 1830. The roughness Reynolds number based on the viscous length scale of the upstream smooth-wall conditions, $k^+ = k / y_*^{\mathrm{SM}}$, is 97 which is close to the fully rough regime. This value of k^+ is in fact a lower bound on the actual value of k^+ because y_* over the roughness is expected to be smaller than y_*^{SM} because the wall shear stress, and hence u_τ, would be enhanced by the roughness. However, an accurate measure of the wall shear stress over the roughness was not available and so the smooth-wall values are used as a baseline. Several thousand PIV realizations are acquired at each condition, ensuring proper convergence of single- and multipoint statistics. Table 1 summarizes the experimental parameters.

Prasad et al. [21] showed that the random error associated with determining particle displacements in PIV is approximately 5% of the particle-image diameter. In the present study, the mean particle-image diameter is approximately 2 pixels, yielding a random error of

0.1 pixels. Therefore, because the time delay between the PIV images for a given experiment (13 μs for cases SM and R1 and 14 μs for case R2) is chosen to yield a bulk displacement of 10–12 pixels, this random error is less than 1% of the full-scale velocity. Furthermore, these random errors do not affect statistics of the velocity because they average to zero for suitably large ensembles like those considered herein. One must also consider two sources of bias error that can appear in PIV measurements. Bias due to loss of image pairs is minimized in the present study since a larger second interrogation window and a bulk window offset are utilized during interrogation of the PIV images. Bias errors due to the peak-locking effect [22] are also minimized in the present experiment because the particle-image diameters exceed 2 pixels [23]. We therefore estimate the bias errors in our PIV measurements at 1% of the full-scale velocity (the reader is directed to Westerweel [23], Christensen and Adrian [24] and Christensen [22] for a more comprehensive discussion of PIV measurement errors).

III.   Results and Discussion

A.   Reynolds-Stress Profiles

Figure 3 presents profiles of the Reynolds stress over smooth and rough walls as a function of wall-normal position. These profiles are computed from velocity ensembles exceeding 3500 statistically independent realizations per condition. The lines in Fig. 3 represent ensemble- and streamwise-averaged profiles for the three cases while the symbols represent the ensemble-averaged profiles for case R2 at the upstream $(x = 7h)$ and downstream $(x = 8h)$ ends of the PIV field of view (to be discussed later). The wall-normal origin for the rough-wall cases is taken to be the mean elevation of the roughness, which is consistent with the streamwise–spanwise plane at which the wall shear stress appears to act ([25], for example), and the upstream smooth-wall friction velocity, u_τ^{SM}, is used to normalize the Reynolds shear stress because an accurate measure of the local shear stress over the roughness was not available. As such, any collapse of the roughness profiles with the smooth-wall data does not imply outer-layer similarity but simply the existence of smooth-wall outer-layer conditions. The mean Reynolds-stress profile from a DNS of a smooth-wall turbulent channel flow [26] at $Re_\tau = 550$ is included in Fig. 3 and comparison with the smooth-wall PIV measurements indicates that the measurements slightly underpredict the mean Reynolds stress close to the wall. This underprediction has been observed previously in PIV studies of smooth-wall channel flow [19,27] and is due to the spatial averaging associated with the coarser grid spacings of the PIV measurement ($\sim 19 y_*$ for the present cases) relative to the much finer grid spacings achievable in DNS (a few y_* close to the wall).

When the smooth-wall profile is compared to the R1 and R2 profiles it is clear that an internal roughness layer has formed given the significant enhancement of the mean Reynolds stress in the presence of the replicated turbine-blade roughness. However, the internal roughness layer only protrudes to $y = 0.35h$, not even halfway to the centerline of the channel, even after nearly eight outer length scales of development downstream. It should be noted that the roughness results well exceed the linear total-stress profile expected
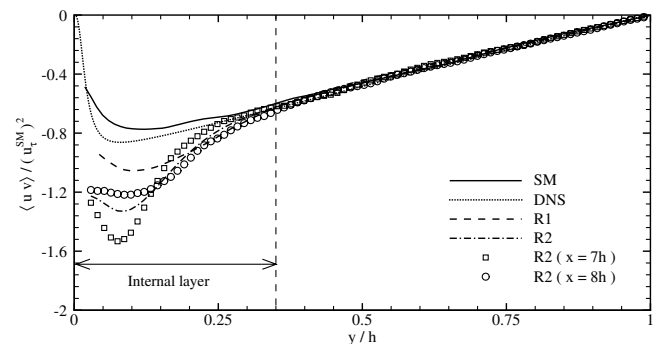
Table 1   Summary of flow parameters for all experiments

Experiment	Re_τ	u_τ^{SM}, m/s	y_*^{SM}, μm	Δ^+	$k^+ = k / y_*^{\mathrm{SM}}$	h/k
SM	1832	1.12	13.9	18.9	——	——
R1	1828	1.12	13.9	19.8	97	18.8
R2	1815	1.12	14.0	21.0	96	18.8

Fig. 3   Mean Reynolds stress as a function of wall-normal position.
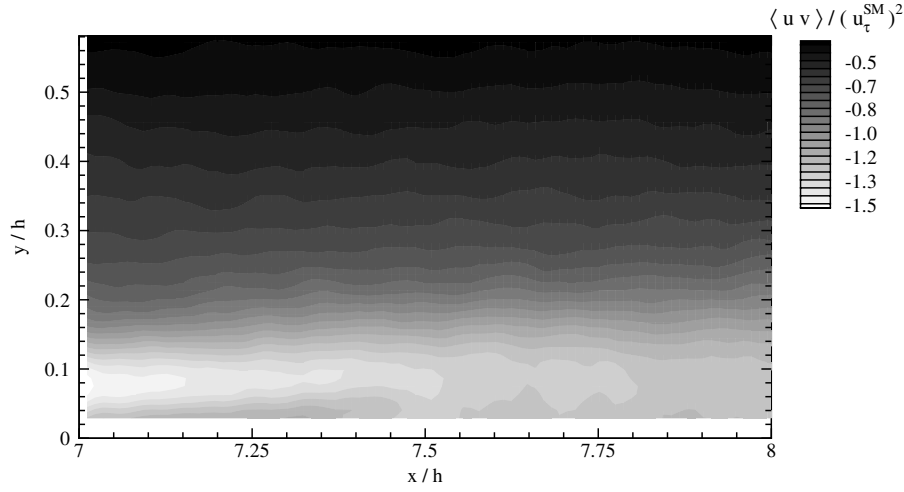
Fig. 4   Ensemble-averaged Reynolds stress for case R2.

in fully developed, smooth-wall turbulent channel flow because they are normalized with the smooth-wall friction velocity (since independent measures of u_τ for the rough-wall cases were not available). Therefore, the fact that the rough-wall profiles exceed the smooth-wall Reynolds-stress and linear total-stress profiles implies that the surface roughness has dramatically increased the local wall shear stress, yielding a commensurate increase in the rough-wall u_τ compared to u_τ^{SM}.

The R2 profiles highlight the strong influence that the local roughness topology can have on the flow. Recalling that the R2 measurements occur just downstream of a distinct step from a deep pocket to a plateau (near $x = 6.75h$ in Fig. 1), the Reynolds stress at $x = 7h$ for case R2 ($\square$ symbols) is significantly enhanced compared to the smooth-wall results, case R1 (relatively fine-scale roughness) and even the R2 profile further downstream at $x = 8h$ ($\bigcirc$ symbols). Examination of the ensemble-averaged Reynolds stress for the R2 case (Fig. 4) indicates that this abrupt step in surface roughness generates a thin, elongated region of intense Reynolds stress near $x = 7h$, with heightened levels of $\langle uv \rangle$ extending at least $1.25h$ downstream of the step. This region of enhanced Reynolds stress is most likely associated with the wake generated by the abrupt, large-scale step in surface roughness noted earlier. This behavior is consistent with what has been observed in studies of arrays of discrete roughness elements where each element generates a wake that contributes significantly to the local flow behavior [28]. As such, dramatic local changes in the surface topology generate flow

modifications that can persist for some appreciable distance downstream. In contrast, these flow modifications do not appear to alter the wall-normal growth of the internal layer since all the roughness profiles collapse onto the smooth-wall result near $y = 0.35h$.

Figure 5 presents probability density functions (PDFs) of uv at $y = 0.1h$, $0.2h$, $0.5h$, and h normalized by the absolute value of the maximum Reynolds stress from the smooth-wall case: $|\langle uv \rangle|_{max}^{SM}$. This value is chosen as a universal normalization so that the relative enhancement of the Reynolds-stress-producing events by the surface roughness can be directly observed. As expected, the PDFs are notably skewed toward negative values for $y = 0.1h$, $0.2h$, and $0.5h$ in both the smooth- and rough-wall cases, consistent with the mean Reynolds-stress profiles shown in Fig. 3. In contrast, symmetry in the uv PDFs is noted at the centerline of the channel where the total mean Reynolds stress is zero. In addition, it is observed that a vast majority of the Reynolds-stress-producing events are quite small in magnitude, whereas only a small number of uv events yield extremely large instantaneous Reynolds shear stress in both the smooth- and rough-wall cases.

Figure 5a indicates that the surface roughness generates a larger number of significant negative uv events at $y = 0.1h$ (within the log layer) compared to the smooth-wall case. This behavior is most notable for case R2 where the largest enhancement of the mean Reynolds stress was observed. In contrast, the number of significant positive uv events increases only slightly in the presence of surface
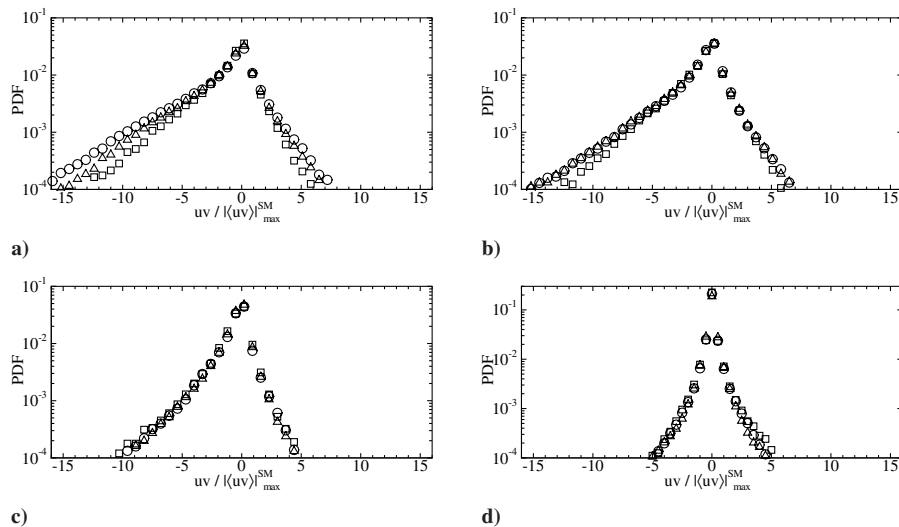

Fig. 5   PDFs of uv normalized by $|\langle uv \rangle|_{max}^{SM}$ at a) $y = 0.1h$, b) $y = 0.2h$, c) $y = 0.5h$, and d) $y = h$. $\square$: SM; $\triangle$: R1; $\bigcirc$: R2. Every fourth point is shown for clarity.
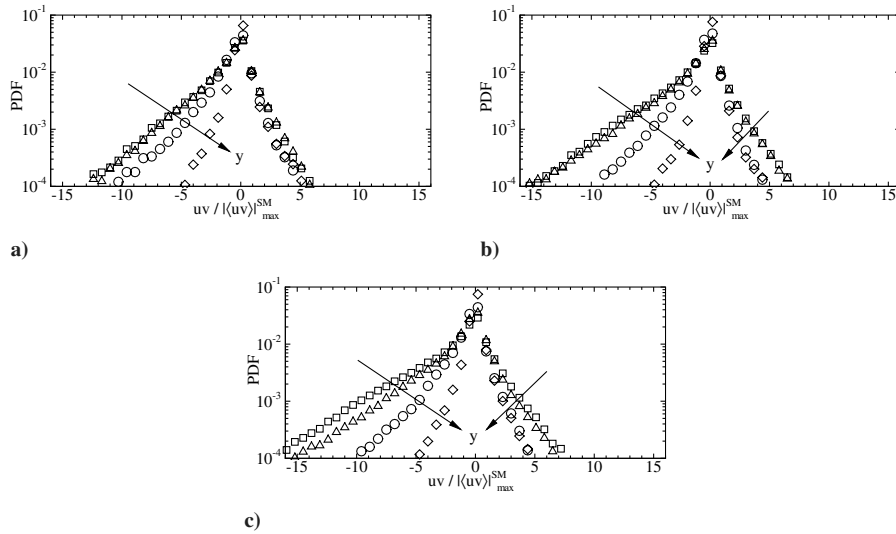
Fig. 6 PDFs of uv normalized by $|\langle uv \rangle|_{\max}^{\mathrm{SM}}$ for a) SM, b) R1, and c) R2. $\square$: $y = 0.1h$; $\triangle$: $y = 0.2h$; $\bigcirc$: $y = 0.5h$; $\diamondsuit$: $y = h$. Every fourth point is shown for clarity.

roughness. Further, the roughness has little effect on both the negative and positive uv events with relatively small magnitude ($uv < 4|\langle uv \rangle|_{\max}^{\mathrm{SM}}$). At $y = 0.2h$ (Fig. 5b), the enhancement of uv by the surface roughness is weaker than at $y = 0.1h$ but still notable in the negative tails of the PDFs. Outside the internal layer at $y = 0.5h$ (Fig. 5c), the PDFs collapse irrespective of the surface condition which is consistent with the collapse of the mean total Reynolds-stress profiles in this wall-normal region (Fig. 3). The PDFs become symmetric at the centerline (Fig. 5d), although uv events several times larger than $|\langle uv \rangle|_{\max}^{\mathrm{SM}}$ can still exist. This latter observation is quite consistent with the results of Sabot and Comte-Bellot [11] for turbulent pipe flow. Taken together, these results suggest that the surface roughness studied herein only alters the tails of the uv PDFs through the generation of significant instantaneous positive and negative uv events, more so the latter than the former, while having little influence on uv events of smaller magnitude.

The PDFs of uv for four wall-normal locations are presented in Figs. 6a–6c for the SM, R1, and R2 cases, respectively. It is interesting to note that the PDFs of positive uv events remain relatively unchanged from the log layer ($y = 0.1h$) to the centerline in the smooth-wall case (Fig. 6a), indicating that the turbulent motions responsible for such contributions maintain their intensities across the outer layer. The same cannot be said of the negative uv events in the smooth-wall case as the negative tails of the uv PDFs show a distinct wall-normal dependence. Similar wall-normal behavior is noted in both roughness cases (Fig. 6b for R1 and Fig. 6c for R2), although the negative and positive uv tails show notable enhancement within the internal roughness layer.

B.   Quadrant Analysis

The results presented in Figs. 3–6 indicate that the surface roughness replicated from a damaged turbine blade yields a net increase in the mean Reynolds stress through the generation of significant, yet highly intermittent, instantaneous negative uv events. However, it is not known whether these negative uv events are associated with an increased number of ejections, sweeps, or both. Likewise, the surface roughness also appears to generate an increased number of significant positive uv events, albeit a much smaller number than the negative uv events, yet it is not clear if this is associated with an increased incidence of outward interactions, inward interactions, or both. Therefore, quadrant analysis is used to identify the dominant contributors to the Reynolds-stress enhancement noted in the presence of surface roughness.

Following Wallace et al. [7] and Lu and Willmarth [8], the mean Reynolds stress at each wall-normal position can be decomposed into contributions from four quadrants ($Q = 1$–4), excluding a hyperbolic hole of size H, as

$$\langle uv \rangle_Q(y) = \frac{1}{M} \sum_{j=1}^{M} u(x_j, y) v(x_j, y) I_Q(x_j, y) \tag{1}$$

where I_Q is the indicator function defined as

$$I_Q(x_j, y) = \begin{cases} 1 & \text{when } |u(x_j, y)v(x_j, y)|_Q \geq H|\langle uv \rangle|_{\max}^{\mathrm{SM}} \\ 0 & \text{otherwise} \end{cases} \tag{2}$$

and M is the total number of vectors at each wall-normal position. Hence, the summation in Eq. (1) represents an ensemble average among statistically independent realizations and a line average in the streamwise direction for a fixed wall-normal location. As noted earlier, a universal threshold $|\langle uv \rangle|_{\max}^{\mathrm{SM}}$ is used to define I_Q so that the enhancement of Reynolds-stress-producing events due to the surface roughness can be clearly identified relative to the smooth-wall case. In addition, a nonzero hole size, H, is used to exclude uv events of small magnitude to determine the relative contributions of the significant uv events identified in the previous section.

Quadrant analysis yields three quantities of interest in assessing the overall contributions of ejections, sweeps, and inward/outward interactions to the mean Reynolds stress:

1) the Reynolds stress contributed by each quadrant for a given H: $\langle uv \rangle_Q(y)$;

2) the stress fraction associated with each quadrant event for a given H:

$$S_Q(y) = \frac{\langle uv \rangle_Q(y)}{\langle uv \rangle(y)} \tag{3}$$

3) the space fraction occupied by each quadrant for a given H:

$$N_Q(y) = \frac{\sum I_Q(y)}{M} \tag{4}$$

Three hole sizes, $H = 0$, 2, and 5, are studied and represent contributions to the total mean Reynolds stress from all, only moderate-to-strong events, and only strong events, respectively. However, only the results for $H = 0$ and $H = 5$ will be presented herein as the $H = 2$ trends are qualitatively similar to those at $H = 5$. Further, the wall-normal trends of these quantities are only presented within the internal layer ($y \leq 0.35h$) where the surface roughness exerts its influence.

Figure 7 presents the Reynolds-stress contributions, $\langle uv \rangle_Q$, from ejections, sweeps, and inward/outward interactions corresponding to $H = 0$ for the smooth and rough cases as a function of wall-normal position. The case $H = 0$ implies that
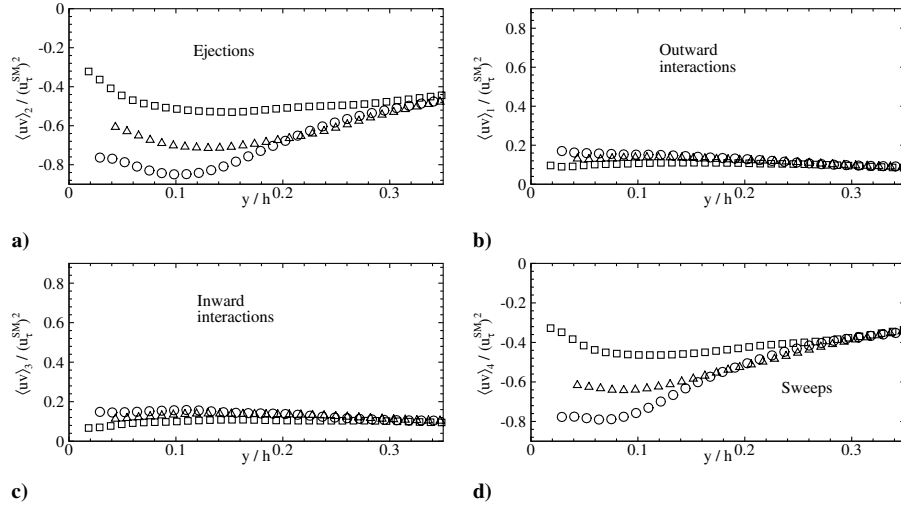
Fig. 7 Contributions of each quadrant to the mean Reynolds stress vs wall-normal position for $H = 0$. a) Ejections; b) outward interactions; c) inward interactions; d) sweeps. $\square$: SM; $\triangle$: R1; $\bigcirc$: R2.

$$\sum_{Q=1}^{4} \langle uv \rangle_Q (y) = \langle uv \rangle(y) \qquad (5)$$

meaning that all contributions to the mean Reynolds stress, intense and weak, are included in this quadrant decomposition. Surface roughness significantly enhances the Reynolds-stress contributions of ejections and sweeps while increasing the contributions from the inward/outward interactions only slightly. The R2 case displays the largest increase in ejection and sweep contributions, consistent with the observations noted earlier. In addition, ejections and sweeps appear to contribute equally to the mean Reynolds stress for $y < 0.1h$; however, for $y > 0.1h$, the contributions from ejections begin to outweigh those from sweeps. As with the total Reynolds-stress profiles presented in Fig. 3, the contributions presented in Fig. 7 are normalized by the smooth-wall friction velocity since measurements of the wall shear stress over the roughness were not available.

While the absolute contributions of Reynolds-stress-producing events, particularly ejections and sweeps, are altered in the presence of surface roughness, the stress fractions for $H = 0$ show little dependence on surface roughness (Fig. 8). In particular, ejections account for roughly 60–70% of the mean Reynolds stress whereas sweeps account for approximately 60% in the region $y \leq 0.35h$ in both the smooth- and the rough-wall cases. The inward and outward interactions generate stress fractions with magnitudes more than 3 times smaller than those of the ejections and sweeps over the same

wall-normal extent. Finally, surface roughness appears to have little influence on the space fractions of the ejections, sweeps, and inward/outward interactions as the smooth- and rough-wall results collapse in the region $y \leq 0.35h$ (Fig. 9). Ejections and sweeps are found to occupy a significant fraction of space in this wall-normal region, accounting for nearly 70% of the events for $H = 0$ irrespective of the surface condition with the remaining 30% associated with inward and outward interactions.

Figure 10 presents the Reynolds-stress contributions from ejections, sweeps, and inward/outward interactions corresponding to $H = 5$ for the smooth and rough cases. The use of $H = 5$ ensures that only the most intense Reynolds-stress-producing events are considered in the quadrant decomposition. For $H = 5$, the contributions from both outward and inward interactions are essentially zero for both the smooth- and the rough-wall cases. In contrast, both ejections and sweeps show clear dependence on the surface conditions as both the R1 and R2 cases yield a significant enhancement of the smooth-wall contributions of such events, most notably in the case of R2. The contributions from ejections are found to be slightly larger than those of sweeps except close to the wall where sweeps contribute slightly more to the overall Reynolds stress compared to ejections. These wall-normal trends are consistent with the recent turbulent-boundary-layer results of Flack et al. [17] over long streamwise fetches of sandpaper and wire mesh.

The dependence of the Reynolds-stress contributions on the surface condition for $H = 5$ is also notable in the stress fractions presented in Fig. 11. The R1 and R2 cases are found to yield ejection
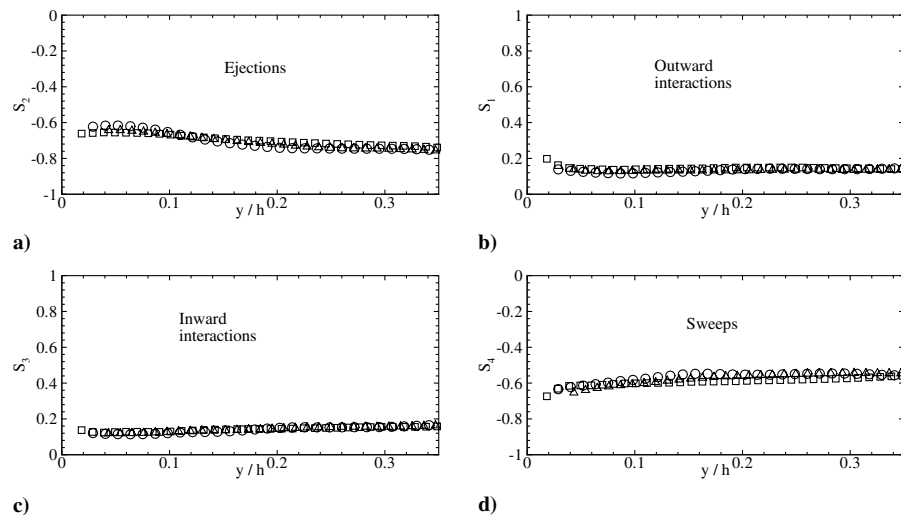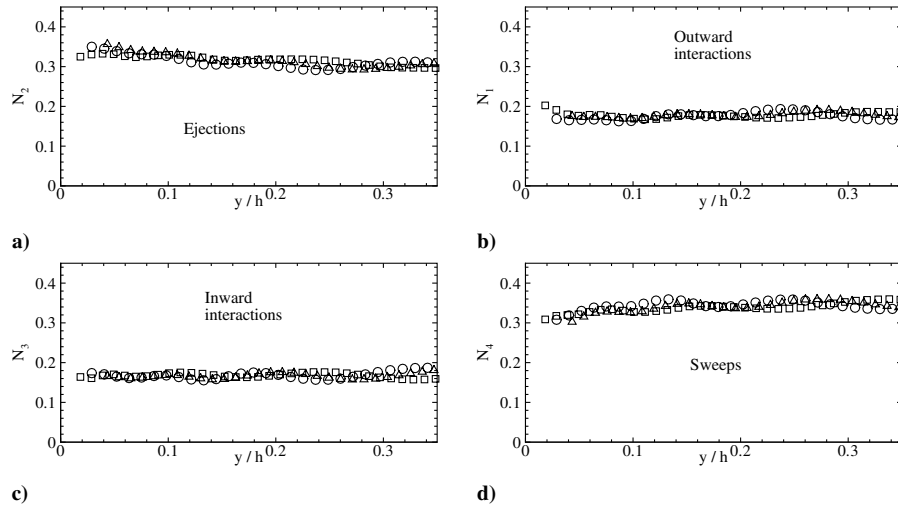

Fig. 8 Stress fractions vs wall-normal position for $H = 0$. a) Ejections; b) outward interactions; c) inward interactions; d) sweeps. $\square$: SM; $\triangle$: R1; $\bigcirc$: R2.

Fig. 9   Space fractions vs wall-normal position for $H = 0$. a) Ejections; b) outward interactions; c) inward interactions; d) sweeps. □: SM; △: R1; ○: R2.
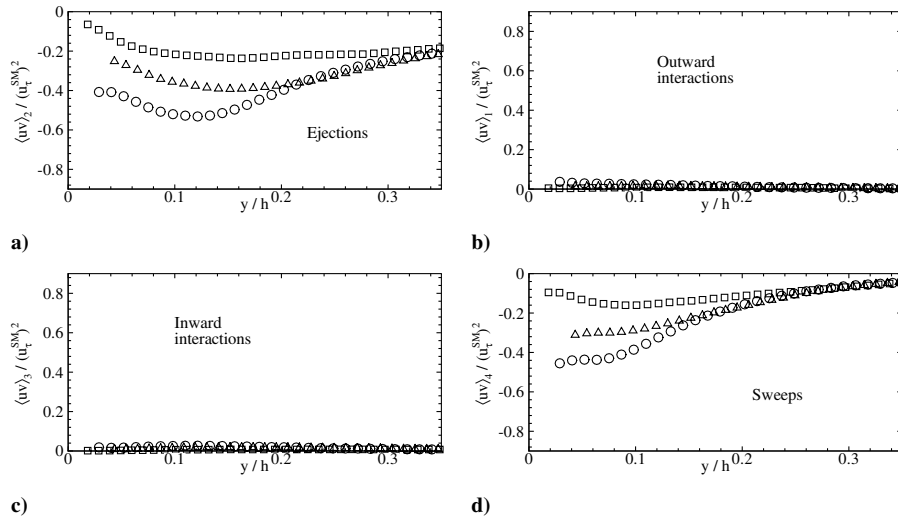

Fig. 10   Contributions of each quadrant to the mean Reynolds stress vs wall-normal position for $H = 5$. a) Ejections; b) outward interactions; c) inward interactions; d) sweeps. □: SM; △: R1; ○: R2.

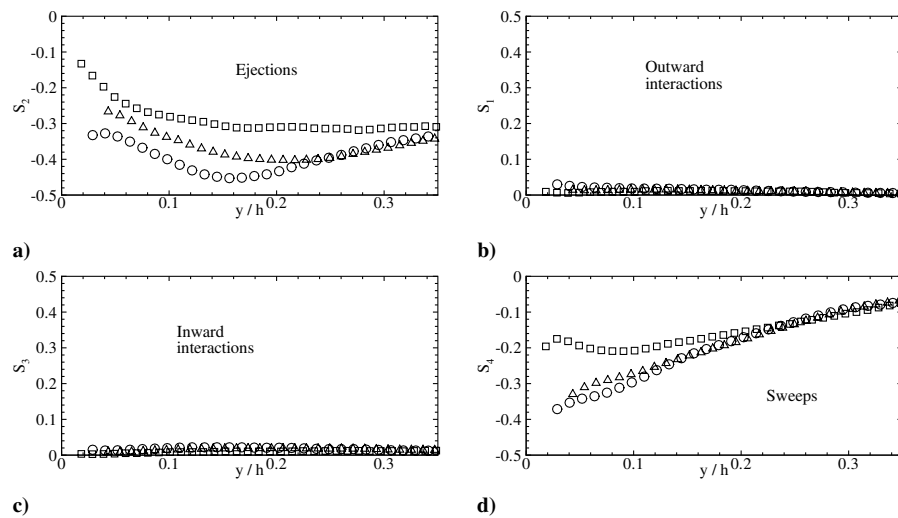**Fig. 11   Stress fractions vs wall-normal position for $H = 5$. a) Ejections; b) outward interactions; c) inward interactions; d) sweeps. □: SM; △: R1; ○: R2.**

stress fractions significantly larger than the smooth-wall case for $y < 0.35h$ while the same rough-wall cases yield enhanced sweep stress fractions for $y < 0.2h$. Therefore, although the stress fractions for $H = 0$ display little sensitivity to the surface conditions, the stress

fractions associated with the most intense uv events display significant dependence on the surface topology. Further, the stress fractions associated with inward/outward interactions are found to be nearly zero for $H = 5$, meaning that the most intense Reynolds-
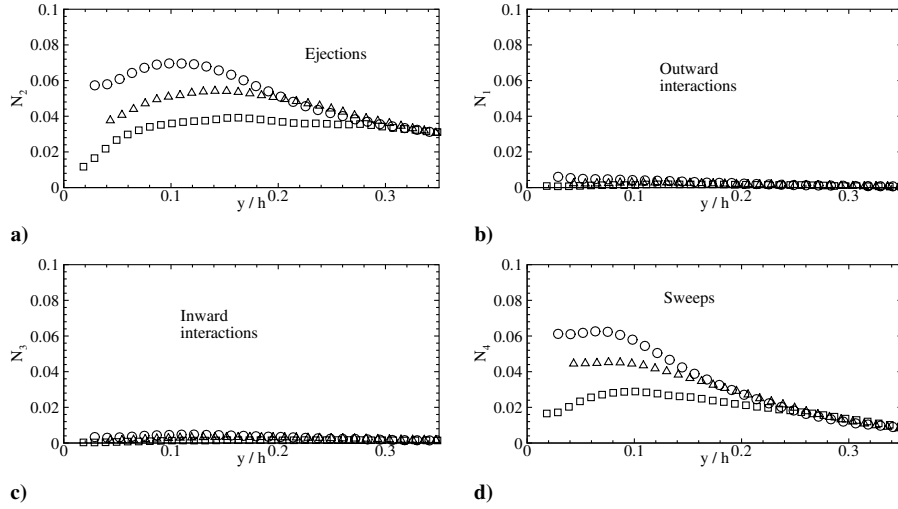
Fig. 12   Space fractions vs wall-normal position for $H = 5$. a) Ejections; b) outward interactions; c) inward interactions; d) sweeps. □: SM; △: R1; ○: R2.

stress-producing events are almost always ejections or sweeps, irrespective of surface condition.

Although ejections and sweeps account for the most intense uv events, they occupy very little physical space (Fig. 12). In particular, although intense ejections and sweeps together account for as much as 70–80% of the mean Reynolds stress (most notably in case R2), these events occupy only a small fraction of space, with the space fraction increasing slightly in the presence of roughness. This slight increase of N_Q in the presence of surface roughness is consistent with the PDFs of uv presented in Fig. 5 which illustrate that surface roughness generates a larger number of significant ejection and sweep events. Most notably, the R2 case generates the largest space fraction for both ejections and sweeps, 3–6%, attributable to the generation of many more intense uv events compared to the smooth-wall case and even the R1 case. Therefore, although the overall ($H = 0$) stress and space fractions are unaffected by the surface conditions, the stress and space fractions of the most intense uv events are strongly correlated with the surface topology as evidenced by the notable differences between the smooth-wall, R1, and R2 cases for $H = 5$.

Finally, the relative contributions of ejections and sweeps as a function of wall-normal position can be quantified by the ratio

$$\alpha(y) = \frac{\langle uv \rangle_2(y)}{\langle uv \rangle_4(y)} \qquad (6)$$

where $\alpha > 1$ and $\alpha < 1$ represent stronger/weaker contributions to the mean Reynolds stress from ejections as compared to sweeps. For $H = 0$ (Fig. 13), α slowly increases from 1 near the wall to nearly 1.4 at the edge of the internal layer ($y = 0.35h$). In addition, α displays no dependence on surface condition as the smooth- and rough-wall results collapse for $H = 0$, consistent with the collapse of the stress and space fractions for $H = 0$ (Figs. 8 and 9). Figure 13b presents α as a function of wall-normal position for $H = 5$. These results suggest that intense ejections dominate over intense sweep events in all regions except the very near-wall region where α is near 1 and are consistent with the observations of Flack et al. [17] over much simpler roughness surfaces (sandpaper and wire mesh). In addition,
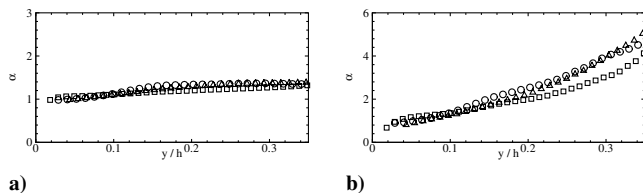
the smooth-wall values of α are observed to be slightly larger for $y < 0.1h$, which is consistent with the dependence of the $H = 5$ stress and space fractions of ejections and sweeps on the surface conditions. This behavior is also consistent with the roughness-sublayer observations of Flack et al. [17]. However, for $y > 0.1h$, this ratio increases slightly in the presence of roughness, indicating a slightly larger contribution from ejections than sweeps at the outer edge of the log layer.

IV.   Conclusions

The dominant Reynolds-stress-producing events in smooth-wall turbulence and turbulence over a short strip of roughness replicated from a damaged turbine blade are found to show significant dependence on the surface conditions. In particular, the mean Reynolds stress is found to increase dramatically, particularly in regions where the surface topology contains large-scale defects. This increase is most likely associated with an enhancement in the overall wall shear stress in the presence of the roughness. Probability density functions of uv indicate that, although positive uv events are relatively unaffected by the presence of surface roughness, the number of intense negative uv events increases dramatically over the roughness. This increased occurrence of intense negative uv events, coupled with the insensitivity of positive uv events to surface roughness, clearly accounts for the dramatic increase in the mean Reynolds stress within the internal layer. Further, the local topology plays a crucial role in the enhancement of the mean Reynolds stress as large-scale surface defects are found to generate significant, but localized, Reynolds-stress-producing events. This latter observation is consistent with the behavior often noted in studies of discrete roughness elements where the wake of each element significantly alters the local flow character [28].

Quadrant analysis reveals that surface roughness significantly increases the overall contributions of ejections and sweeps to the mean Reynolds stress compared to the smooth-wall case. In contrast, the inward and outward interaction contributions remain relatively unchanged in the presence of surface roughness. For $H = 0$, the stress and space fractions of ejections, sweeps, and inward/outward interactions are found to be insensitive to the surface topology. This behavior is consistent with the PDFs of uv events which showed clear insensitivity to the surface conditions for weak negative and positive uv events. In contrast, the most intense uv events generate stress and space fractions that show strong dependence on the surface topology, indicating that the increase in the mean Reynolds stress is directly attributable to the generation of extremely intense, yet highly intermittent, ejections and sweeps.

Finally, the fact that the $H = 0$ stress/space fractions and α display little sensitivity to the surface topology indicates that the flow over

Fig. 13   Ratio of ejection to sweep contributions vs wall-normal position for a) $H = 0$ and b) $H = 5$. □: SM; △: R1; ○: R2.

the replicated turbine-blade roughness and smooth-wall turbulence may indeed be similar in the spirit of outer-layer similarity. If this is indeed the case, then the intense uv events, which display significant dependence on surface topology, may play a role in defining the enhanced wall shear stress over the roughness. Further, given that many of the trends noted herein are consistent with other studies over idealized roughness (sandgrain, discrete elements, etc.), such studies may in fact be sufficient for describing the influence of highly irregular surface conditions on the flow. An accurate measure of the wall shear stress over the rough surface would be needed to confirm these conjectures and such a measure was unfortunately not available in the present experiments. Finally, the present short-fetch observations cannot be regarded as *quantitatively* representative of flow over much longer fetches of highly irregular surface roughness. However, the *qualitative* consistency between the present observations and the aforementioned studies of idealized roughness over long fetches in the fully rough regime ($k^+ > 90–100$; high Re_τ) suggests that the present results may at least retain qualitative consistency with fully rough flow over longer streamwise fetches of highly irregular roughness. Direct assessment of this possibility is required.

Acknowledgments

References

[1] Smits, A. J., and Wood, D. H., "The Response of Turbulent Boundary Layers to Sudden Perturbations," *Annual Review of Fluid Mechanics*, Vol. 17, 1985, pp. 321–58.

[2] Antonia, R. A., and Luxton, R. E., "The Response of a Turbulent Boundary Layer to a Step Change in Surface Roughness. Part 1. Smooth to Rough," *Journal of Fluid Mechanics*, Vol. 48, 1971, pp. 721–761.

[3] Andreopoulos, J., and Wood, D. H., "The Response of a Turbulent Boundary Layer to a Short Length of Surface Roughness," *Journal of Fluid Mechanics*, Vol. 118, 1982, pp. 143–164.

[4] Bons, J. P., Taylor, R. P., McClain, S. T., and Rivir, R. B., "The Many Faces of Turbine Surface Roughness," *Journal of Turbomachinery*, Vol. 123, No. 4, 2001, pp. 739–748.

[5] Bons, J. P., "St and C_f Augmentation for Real Turbine Roughness with Elevated Freestream Turbulence," *Journal of Turbomachinery*, Vol. 124, No. 4, 2002, pp. 632–644.

[6] Karlsson, R. I., "Studies of Skin Friction in Turbulent Boundary Layers on Smooth and Rough Walls," Ph.D. Thesis, Department of Allied Thero and Fluid Dynamics, Chalmers University of Technology, Göteborg, Sweden, 1980.

[7] Wallace, J. M., Eckelmann, H., and Brodkey, R. S., "The Wall Region in Turbulent Shear Flow," *Journal of Fluid Mechanics*, Vol. 54, 1972, pp. 39–48.

[8] Lu, S. S., and Willmarth, W. W., "Measurements of the Structure of the Reynolds Stress in a Turbulent Boundary Layer," *Journal of Fluid Mechanics*, Vol. 60, 1973, pp. 481–511.

[9] Wallace, J. M., and Brodkey, R. S., "Reynolds Stress and Joint Probability Density Distributions in the *u-v* Plane of a Turbulent Channel Flow," *Physics of Fluids*, Vol. 20, No. 3, 1977, pp. 351–355.

[10] Teitel, R., and Antonia, R. A., "The Interaction Region of a Turbulent Duct Flow," *Physics of Fluids A*, Vol. 2, No. 5, 1990, pp. 808–813.

[11] Sabot, J., and Comte-Bellot, G., "Intermittency of Coherent Structures in the Core Region of Fully Developed Turbulent Pipe Flow," *Journal of Fluid Mechanics*, Vol. 74, 1976, pp. 767–796.

[12] Grass, A. J., "Structural Features of Turbulent Flow over Smooth and Rough Boundaries," *Journal of Fluid Mechanics*, Vol. 50, 1971, pp. 233–255.

[13] Raupach, M. R., "Conditional Statistics of Reynolds Stress in Rough-Wall and Smooth-Wall Turbulent Boundary Layers," *Journal of Fluid Mechanics*, Vol. 108, 1981, pp. 363–382.

[14] Krogstad, P. A., Antonia, R. A., and Browne, L. W. B., "Comparison Between Rough and Smooth-Wall Turbulent Boundary Layers," *Journal of Fluid Mechanics*, Vol. 245, 1992, pp. 599–617.

[15] Demare, S., Labraga, L., and Tournier, C., "Comparison and Scaling of the Bursting Period in Rough and Smooth Walls Channel Flows," *Journal of Fluids Engineering*, Vol. 121, No. 4, 1999, pp. 735–745.

[16] Krogstad, P.-A., Andersson, H. I., Bakken, O. M., and Ashrafian, A., "An Experimental and Numerical Study of Channel Flow with Rough Walls," *Journal of Fluid Mechanics*, Vol. 530, 2005, pp. 327–352.

[17] Flack, K. A., Schultz, M. P., and Shapiro, T. A., "Experimental Support for Townsend's Reynolds Number Similarity Hypothesis on Rough Walls," *Physics of Fluids*, Vol. 17, No. 3, 2005, pp. 035102-1–035102-9.

[18] Nakagawa, S., and Hanratty, T. J., "Influence of a Wavy Boundary on Turbulence. II. Intermediate Roughened and Hydraulically Smooth Surfaces," *Experiments in Fluids*, Vol. 35, No. 3, 2003, pp. 437–447.

[19] Christensen, K. T., "Experimental Investigation of Acceleration and Velocity Fields in Turbulent Channel Flow," Ph.D. Thesis, Department of Theoretical and Applied Mechanics, University of Illinois at Urbana–Champaign, Urbana, IL, 2001.

[20] Christensen, K. T., and Adrian, R. J., "Statistical Evidence of Hairpin Vortex Packets in Wall Turbulence," *Journal of Fluid Mechanics*, Vol. 431, 2001, pp. 433–443.

[21] Prasad, A. K., Adrian, R. J., Landreth, C. C., and Offutt, P. W., "Effect of Resolution on the Speed and Accuracy of Particle Image Velocimetry Interrogation," *Experiments in Fluids*, Vol. 13, Nos. 2–3, 1992, pp. 105–116.

[22] Christensen, K. T., "The Influence of Peak-Locking Errors on Turbulence Statistics Computed from PIV Ensembles," *Experiments in Fluids*, Vol. 36, No. 3, 2004, pp. 484–497.

[23] Westerweel, J., "Fundamentals of Digital Particle Image Velocimetry," *Measurement Science and Technology*, Vol. 8, No. 12, 1997, pp. 1379–1392.

[24] Christensen, K. T., and Adrian, R. J., "Measurement of Instantaneous Eulerian Acceleration Fields by Particle-Image Accelerometry: Method and Accuracy," *Experiments in Fluids*, Vol. 33, No. 6, 2002, pp. 759–769.

[25] Jackson, P. S., "On the Displacement Height in the Logarithmic Velocity Profile," *Journal of Fluid Mechanics*, Vol. 111, No. 6, 1981, pp. 15–25.

[26] del Alamo, J. C., and Jimenez, J., "Spectra of the Very Large Anisotropic Scales in Turbulent Channels," *Physics of Fluids*, Vol. 15, 2003, pp. L41–L44.

[27] Liu, Z.-C., Landreth, C. C., Adrian, R. J., and Hanratty, T. J., "High Resolution Measurement of Turbulent Structure in a Channel with Particle Image Velocimetry," *Experiments in Fluids*, Vol. 10, No. 6, 1991, pp. 301–312.

[28] Tomkins, C. D., "The Structure of Turbulence over Smooth and Rough Walls," Ph.D. Thesis, Department of Theoretical and Applied Mechanics, University of Illinois at Urbana–Champaign, Urbana, IL, 2001.